Draft Version 1; May 7, 2015
Preprint typeset using LaTeX style emulateapj v. 11/10/09

RESONANT ORBITS AND THE HIGH VELOCITY PEAKS TOWARDS THE BULGE

Matthew Molloy
Kavli Institute for Astronomy & Astrophysics, Peking University,
Yi He Yuan Lu 5, Hai Dian Qu, Beijing 100871, China (matthewmolloy@gmail.com)

Martin C. Smith
Key Laboratory for Research in Galaxies and Cosmology, Shanghai Astronomical Observatory,
Chinese Academy of Sciences, 80 Nandan Road, Shanghai 200030, China (msmith@shao.ac.cn)

N. Wyn Evans
Institute of Astronomy, Madingley Road, Cambridge, CB3 0HA, UK (nwe@ast.cam.ac.uk)

Juntai Shen
Key Laboratory for Research in Galaxies and Cosmology, Shanghai Astronomical Observatory,
Chinese Academy of Sciences, 80 Nandan Road, Shanghai 200030, China (jshen@shao.ac.cn)
Draft Version 1; May 7, 2015

ABSTRACT

We extract the resonant orbits from an N-body bar that is a good representation of the Milky Way, using the method recently introduced by Molloy et al. (2015). By decomposing the bar into its constituent orbit families, we show that they are intimately connected to the boxy-peanut shape of the density. We highlight the imprint due solely to resonant orbits on the kinematic landscape towards the Galactic centre. The resonant orbits are shown to have distinct kinematic features and may be used to explain the cold velocity peak seen in the APOGEE commissioning data (Nidever et al. 2012). We show that high velocity peaks are a natural consequence of the motions of stars in the 2:1 orbit family. The locations of the peaks vary with bar angle and, with the tacit assumption that the observed peaks are due to the 2:1 family, we find that the locations of the high velocity peaks correspond to bar angles in the range $10^\circ < \theta_{\rm bar} < 25^\circ$. However, some important questions about the nature of the peaks remain, such as their apparent absence in other surveys of the Bulge and the deviations from symmetry between equivalent fields in the north and south.
Subject headings: Galaxy: kinematics and dynamics — Galaxy: evolution

1. INTRODUCTION

It is now widely accepted that the Milky Way (MW) hosts a bar. Many methods have been used to map out the structure of the bar, such as IR photometry (Blitz & Spergel 1991; Dwek et al. 1995), gas dynamics (Englmaier & Gerhard 1999; Weiner & Sellwood 1999), star counts (López-Corredoira et al. 2007; Robin et al. 2012), microlensing (Udalski et al. 1994; Evans & Belokurov 2002; Wyrzykowski et al. 2015) and even the local kinematic landscape (Dehnen 1999, 2000). The MW bar exhibits a boxy-peanut shape (e.g., Dwek et al. 1995), which is host to an X-shaped structure (Nataf et al. 2010; Saito et al. 2011; Li & Shen 2012; Ness et al. 2012). The spatial density of the bar has been mapped out most recently in red clump stars from OGLE-III and the VVV data (e.g., Wegg & Gerhard 2013; Cao et al. 2013). However, despite a number of radial velocity surveys toward the Galactic bulge, kinematic substructure has rarely been observed. This is a pity, as such substructure may betray evidence of the processes that formed and shaped the bar. The Bulge RAdial Velocity Assay (BRAVA; Rich et al. 2007) and GIRAFFE Inner Bulge Survey (GIBS; Zoccali et al. 2014) both observed ∼10,000 giants over a large region of the bulge, but revealed no signature of cold streams. The ARGOS survey (see Ness & Freeman 2012; Ness et al. 2013) has also yet to reveal evidence for streams in the bulge, although their velocity distributions, cut according to metallicity, hint at the wealth of information contained in the kinematic data.

Recently, however, a cold high velocity stream has been observed by Nidever et al. (2012) in the Apache Point Observatory Galactic Evolution Experiment (APOGEE) commissioning data. For certain fields towards the Galactic Bulge, they find bimodal velocity distributions and identify cold ($\sigma \sim 20$ km s^{-1}) secondary peaks in the distribution of line of sight velocities at $v_{\rm los} \sim 200$ km s^{-1}. The independent observations of Babusiaux et al. (2014) also hint at the presence of a high velocity peak, this time with red clump stars. The origin, and even the existence, of this feature has been the subject of recent debate (Li et al. 2014; Zoccali et al. 2014). Li et al. (2014) found the absence of a statistically significant cold high velocity peak in two N-body barred models. They also showed that it is possible for a spurious high velocity peak to appear if there are only a limited number of stars observed. Here, we look at the matter anew, using novel algorithms to extract nearly periodic orbits from bar simulations.

2. ORBITAL COMPONENTS IN THE BAR

In Molloy et al. (2015, hereafter M15), we introduced a method to identify resonant orbits in N-body simulations, and used it to provide a possible explanation for the bimodal velocity distributions observed towards the Galactic anti-Centre. The same method is now applied to the inner parts of a barred model of the Milky Way. Here, a cold but thickened disc self-consistently develops a bar, which undergoes a buckling instability to form a Bulge that is a good match to that of the Milky Way (see Shen et al. 2010; Li & Shen 2012). Resonant orbits can be characterized by the fact that they close and return to a previously occupied location in phase space in some rotating frame. The method in M15 proceeds by recalculating the N-body orbits in many different rotating frames. We define a metric $D_{\rm ps}$ to measure

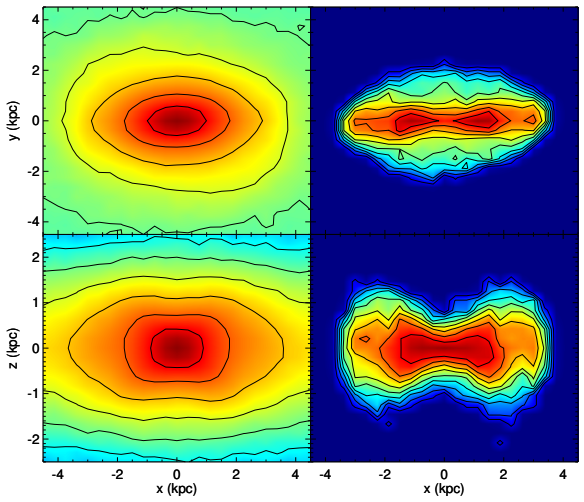

Figure 1. The surface density in the x-y (top) and x-z (bottom) planes for all (left) and 2:1 resonant orbits (right).

the distance each particle travels from some arbitrarily chosen starting point in the rotating frame. If an orbit almost closes, $D_{\rm ps}$ should, at some point along its trajectory, be nearly zero. By defining a cut-off, we can extract a sample of the nearly closed orbits from the simulation. Resonant orbits can librate about each family's parent orbit, so by defining tighter and tighter cuts on $D_{\rm ps}$, we can extract cleaner and cleaner samples of resonant orbits. The choice of cut on $D_{\rm ps}$ is really set by the problem in hand.

We make some minor modifications to the algorithm described in M15. In bars, there are always some chaotic orbits, especially near corotation. Chaotic orbits may return arbitrarily close to their chosen starting point over long timescales (the Poincaré Recurrence Theorem), and can therefore be mistaken as periodic. Previously, we measured the phase space distance from a single point as the orbit proceeded on its trajectory over $\sim$ 1 Gyr. Here, we define a time frame, unique to each particle, over which we apply the phase space distance method. For each particle, we measure the duration it takes to complete eight radial oscillations. This ensures that we have a long enough trajectory to extract high-order periodic orbits while excluding chaotic orbits that rapidly explore their phase space volume. For orbits very close to the centre, this time frame may be sampled by very few points so we interpolate the trajectory.

Also, instead of measuring the phase space distance from a single point, we find the time at which a particle reaches its first apocentre, t_0. As we scan different rotating frames (between $37 \leq \Omega_{\rm p} \leq 40$ km/s/kpc), we extract sections of the trajectories that lie in the range $\phi'(t_0)$ to $\phi'(t_0) + \pi/4$, where ϕ' is the azimuthal angle in the rotating frame. This gives us, say, n similar sections of the trajectory. If n is less than three, then we increase the duration over which we apply the method. The $n = 1$ section is the reference section which we compare to following test sections. The phase space distance $D_{\rm ps}$ is measured between successive points on the reference section and the test sections. We take the average $D_{\rm ps}$ between the orbit sections as a measure of how "closed" the orbit is - the lower the value, the more closed the orbit. Of the $n - 1$ $D_{\rm ps}$ values, we take the minimum and in the following we adopt a cut on the phase space distance of $D_{\rm ps} < 0.06$ (Over the course of an orbit $D_{\rm ps}$ varies between $0 < D_{\rm ps} < \sqrt{2}$, see M15).

By extracting a sample of resonant orbits in the central regions, we can deduce the contribution they make to the structure of the bar. Figure 1 shows the normalized surface density of the inner parts of the disc. In the left panels, we show the x-y (top) and x-z (bottom) surface density for all of the particles in the simulation. The bar extends to $\sim$4 kpc or $R_{\rm CR}/a \approx 1.125$ and has an axis ratio of $b/a \approx 0.5$. This is slightly less extended than the value of 0.35 found by OGLE (Rattenbury et al. 2007) but agrees well with the structure derived recently from a large sample RR Lyrae (Pietrukowicz et al. 2014). The x-z surface density exhibits a strong boxy-peanut shape characteristic of buckled bars. We extract the resonant 2:1 orbits by estimating the azimuthal (Ω) and epicyclic (κ) frequencies for our sample of closed orbits. For each orbit, we calculate $q = (\Omega - \Omega_{\rm p})/\kappa$, where $\Omega_{\rm p}$ is the pattern speed of the frame in which the orbit closes, or reaches its lowest $D_{\rm ps}$. We then extract the 2:1 orbits as those having $0.48 \leq q \leq 0.52$. The surface densities are shown in the right panels of Figure 1. It is clear that the 2:1 orbits generate the backbone of the bar. The buckling instability has a noticeable effect on this family of orbits, inducing a large vertical velocity dispersion for stars at the end of the bar. The contribution of the 2:1 family to the boxy and peanut shape is unmistakable.

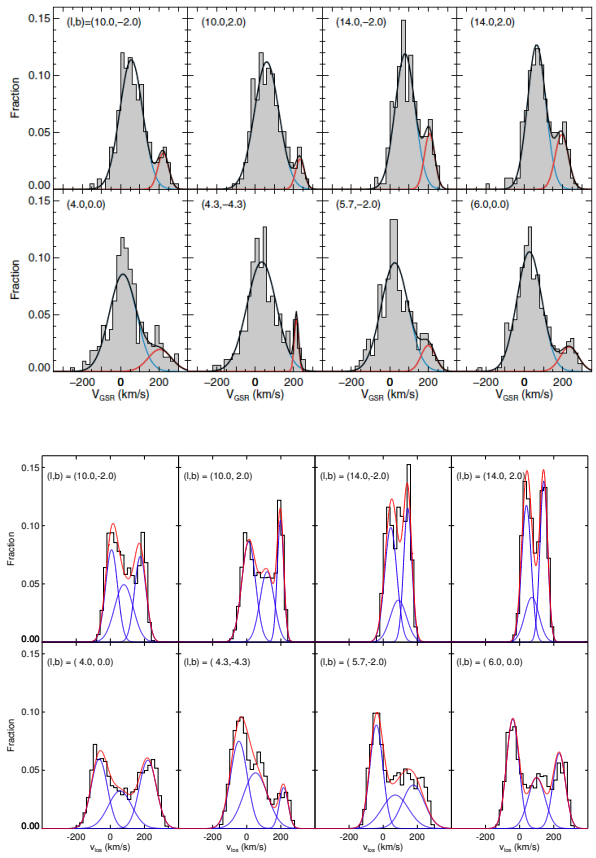

Figure 2. Top: For convenience, we show the $v_{\rm los}$ distributions taken from Nidever et al. (2012). **Bottom:** The $v_{\rm los}$ distributions for the sample of 2:1 resonant orbits in each field, assuming a bar angle of 15°. We use a genetic algorithm to populate 3-Gaussian mixture models for the data.

3. VELOCITY DISTRIBUTIONS

The photometry and star counts for this model have already been shown to be a good match to observations. Indeed, the simulation was tailored to match the kinematics towards the Galactic Bulge as seen by the BRAVA data (Shen et al. 2010). Since we can deconstruct the bar into its different orbital families, we can now characterize the contribution of each family to the velocity distributions. The APOGEE commissioning data revealed cold high velocity peaks for a number of Bulge

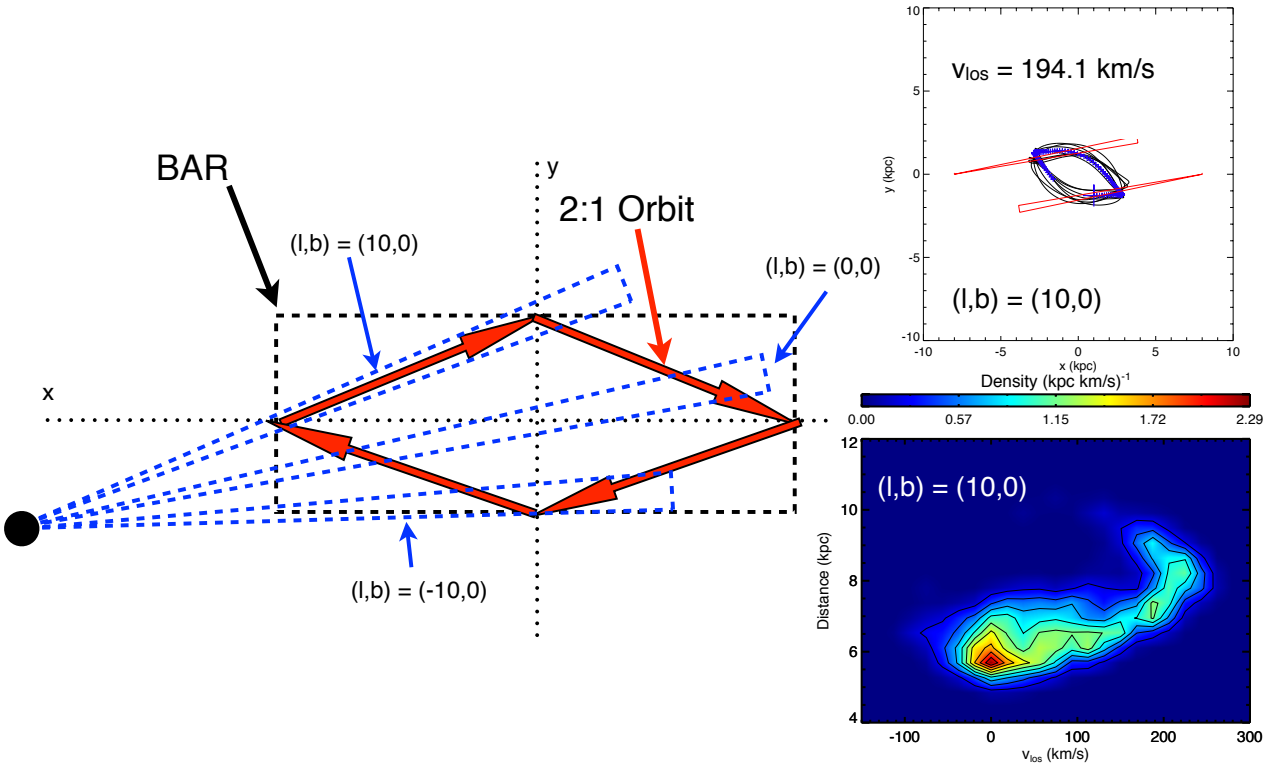

Figure 3. A schematic (and simplified) representation of a 2:1 bar orbit. The red arrows represent the motion of the particle in the frame of the bar (the black dashed box). For different fields, represented by the blue dashed lines, it is clear that this type of orbit gives different contributions to the line of sight velocities. For $l > 0°$, we expect the star to be moving away, whilst the reverse is true for fields with $l < 0°$. **Inset, top right:** A sample orbit from a high velocity peak at $(l, b) = (10, 0)$, the red triangles indicate the fields of view from equivalent sides of the disc. The blue dots represent the preceding 100 timesteps of the orbit and the large blue cross, inside the field of view, indicates the position of the particle when it has a high $v_{\rm los}$ (listed). **Inset, bottom right:** The density of the 2:1 resonant orbits in the field at $(l, b) = (10, 0)$ as a function of $v_{\rm los}$ and distance. The highest velocity particles lie at a distance of ~ 8.5 kpc corresponding to pericentric passage. The lowest velocity particles lie at a distance of ~ 6 kpc corresponding to apocentric passage.

fields. Below we will show that that these peaks arise naturally as a result of the motions of resonant bar orbits, in particular, the 2:1 orbital family. We should note here that, if we include all simulation particles in our line of sight velocity distributions we recover the result of Li et al. (2014) where no cold peaks are revealed.

To generate mock $v_{\rm los}$ distributions, we first fix some fundamental parameters. We choose the Solar radius as $R_\odot = 8.5$ kpc and the circular velocity at $R_\odot$ as $v_{\rm c} = 220$ km s^{-1}. Varying these between reasonable values has only minor effects on the distributions. We assume an angle between the long axis of the bar and the Solar–Galactic Centre (GC) line of $\theta_{\rm bar} = 15°$ (we later justify the choice, where we explore a range of bar angles). We also limit the distances of the particles to between 3 kpc and 9 kpc and, in order to increase the numbers in the samples, we include particles from equivalent positions on either side of the disc and increase the diameter of the field by a factor of two compared to the APOGEE fields. As a further measure to increase the number of particles, we also average over 10 timesteps, making sure to take into account the (small) change in bar angle between timesteps.

The top panel of Figure 2 shows the kinematic data on the APOGEE commissioning fields of Nidever et al. (2012), together with their two Gaussian decomposition. In the bottom plot of Figure 2, we show the velocity distributions for our sample of 2:1 orbits. To avoid forcing fits to binned data, we instead opt for a more general approach. We populate Gaussian mixture models (GMMs) using a genetic algorithm that converges on probability distribution functions that could have produced the data[1]. This only requires one to input the range of parameter space to explore. In order to compare the fits across each field, we force the distributions to be fit with three Gaussians. Initially, we fit each of the field's distributions with one to five Gaussians. We then performed likelihood ratio tests to see when adding an extra Gaussian component made no significant improvement. Most of the fields preferred either two (43.75%) or three (52.5%) Gaussians, while only a small proportion preferred one Gaussian (3.75%). Generally, the distributions are split into negative and positive velocity components, with an intermediate component in some fields. We interpret the negative velocity component as being due to particles on the near side of the bar, streaming towards apocentre. The high velocity component are then the particles streaming towards pericentre on the far side of the bar, while the intermediate component represents the particles that are slowing down as they approach apocentre, those at apocentre (with almost zero line-of-sight velocity) and those leaving apocentre, speeding up as they head towards pericentre. The shape, and number of components in the distribution is a non-trivial function of the field being observed, the chosen bar angle and the range of distances being sampled. For a selection of bar angles, we list the values of the peaks of the distributions for each field in Table 1. In the case of the three Gaussian fits to the 2:1 distributions, we list the highest valued peaks.

A crude representation of a 2:1 bar orbit is shown in Figure 3. The orbit, shown as the red arrows, reaches its apocentre

[1]We do this using the freely available SOLBER routines: http://www.ast.cam.ac.uk/∼vasily/solber/

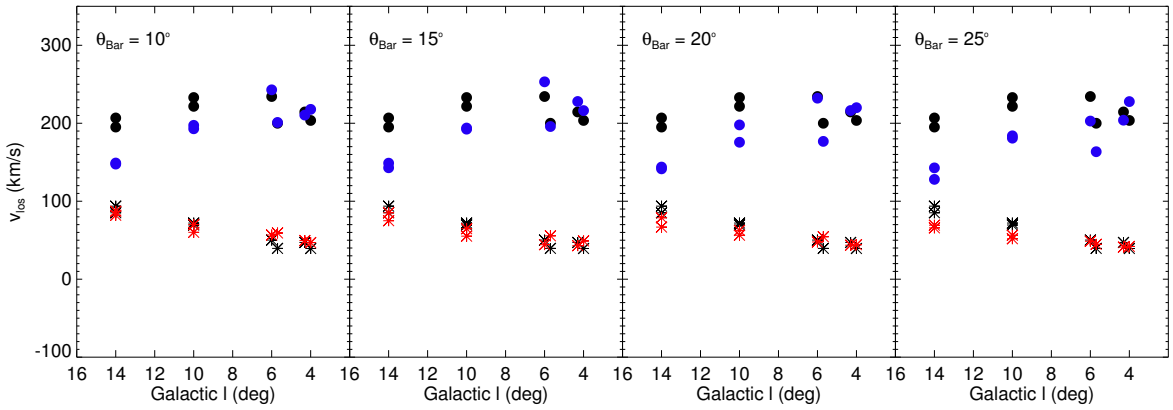

Figure 4. For the APOGEE commissioning fields shown in Nidever et al. (2012), we use Gaussian mixture models to characterize the $v_{\rm los}$ distributions assuming bar angles in the range $5^\circ \leq \theta_{\rm bar} \leq 50^\circ$ (shown here is $10^\circ \leq \theta_{\rm bar} \leq 25^\circ$). The black stars/dots represent the general/high velocity peaks seen in the APOGEE data. The blue dots are the highest velocity peaks from our Gaussian mixture models for the 2:1 orbit velocity distributions. The red stars are the peaks from χ^2 fits to all particles in the fields.

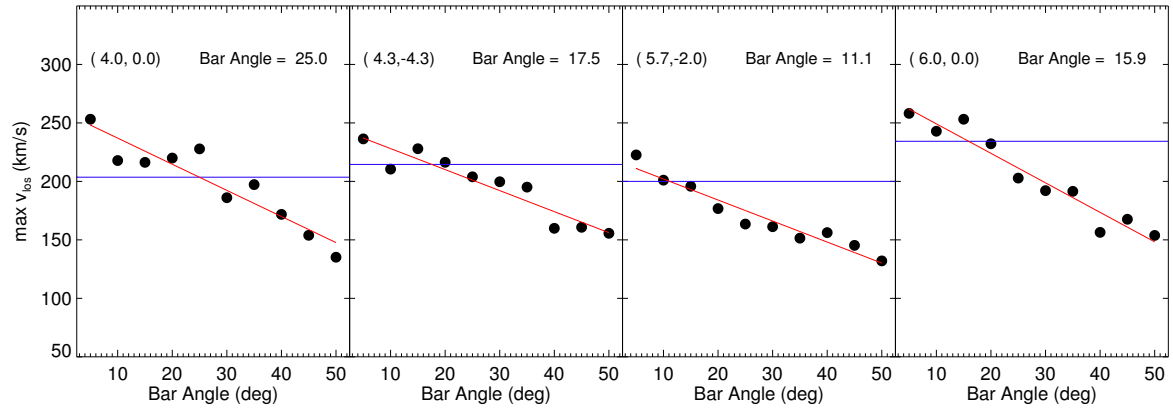

Figure 5. The high velocity peaks from each field with $l < 10^\circ$ plotted as a function of the assumed bar angle (i.e., the blue dots from Figure 4). For each field, the high velocity peak from the APOGEE commissioning data is indicated by the blue horizontal line. A linear fit is made to the peaks and shown as the red line. The bar angle is assumed to the point of intersection of the lines and is listed in each panel.

at each end of the bar (on the x-axis), while the pericentres are located in the directions perpendicular to the bar (the black dashed box). The black dot represents the position of the Sun, so that the bar is rotating in a clockwise direction and the Galactic Centre-Solar position line is at an angle close to 20° with respect to the bar. The dashed blue lines indicate the fields of view in Galactic coordinates. With $(l, b) = (10^\circ, 0^\circ)$, we can see how this type of orbit contributes to a high velocity component in this direction. For this line-of-sight, the measured $v_{\rm los}$ captures most of the components of Galactocentric $v_{\rm R}$ and v_ϕ and results in the high velocity peaks shown in Figure 2. In the Galactocentric frame, these stars have $v_{\rm R} < 0$ km s^{-1} and $v_\phi \ll 0$ km s^{-1} which, for this particular direction in relation to the Solar position, make a significant contribution to $v_{\rm los}$ – in fact, almost all of the particle's velocity is coincident with the line of sight.

As a specific example, we take a sample orbit in the direction of $(l, b) = (10^\circ, 0^\circ)$ from the high velocity component ($v_{\rm los} > 150$ km s^{-1}) in the velocity distributions assuming a bar angle of 20°. We plot the orbit in the upper right panel of Figure 3 and indicate with the red lines the fields of view from which our sample is derived. The orbits are plotted over a period of ∼1 Gyr with the final 100 timesteps indicated with blue crosses and the final timestep shown as the large blue cross lying inside the field of view. The line of sight velocity, assuming a Solar position of $(x, y) = (8.5, 0)$, is also listed.

A population of circular orbits (if they exist in this region) would make a similar, but smaller, contribution to the high velocity peak in $v_{\rm los}$ since $v_{\rm R} \approx 0$ km s^{-1}. This direction also captures stars that are just reaching their maximum radius and so contribute to the negative velocity component in the distributions of $v_{\rm los}$. The peaks of this component are at a lower velocity compared to the simple disc rotation model. This shows that resonant orbits in this direction imprint both low and high velocity kinematic signatures on the line of sight velocity distributions. A field centered on $(l, b) = (0^\circ, 0^\circ)$ passes through the whole structure of the bar and therefore catches stars with a negative $v_{\rm los}$ on the near side and with positive $v_{\rm los}$ on the far side. At negative l, the bar stars are approaching the Solar position and so imprint a high negative velocity component, mirroring the corresponding fields at positive l. Having a non-zero bar angle influences the differing shapes of the distributions between positive and negative longitude fields.

The lower right panel of Figure 3 shows the density of particles as a function of $v_{\rm los}$ and distance. For the line of sight $(l, b) = (10^\circ, 0^\circ)$, particles that are reaching apocentre contribute to the peak at ~ 0 km s^{-1} and are at smaller distances

Table 1
Line-of-sight velocity distributions.

(l,b) (°)	$\theta_{\rm bar}$	All Peak[a] km s^{-1}	2:1 Peak[b] km s^{-1}
(10.0,-2.0)	10°	60.2	192.9
	15°	55.2	192.4
	20°	56.3	175.6
	25°	51.9	180.9
(10.0,2.0)	10°	70.1	197.3
	15°	64.7	193.9
	20°	62.5	197.7
	25°	56.3	183.9
(14.0,-2.0)	10°	82.0	149.0
	15°	75.0	148.8
	20°	66.8	143.8
	25°	65.8	128.0
(14.0,2.0)	10°	87.1	147.6
	15°	85.2	142.9
	20°	78.8	141.5
	25°	69.3	142.8
(4.0,0.0)	10°	47.0	217.8
	15°	49.1	216.3
	20°	44.2	220.0
	25°	42.0	227.8
(4.3,-4.3)	10°	49.6	210.5
	15°	43.0	227.9
	20°	43.6	216.3
	25°	41.1	203.9
(5.7,-2.0)	10°	59.3	201.0
	15°	55.6	195.1
	20°	54.5	176.7
	25°	44.8	163.5
(6.0,0.0)	10°	56.7	242.9
	15°	44.3	253.1
	20°	47.8	232.2
	25°	48.7	202.8

[a] χ^2 fits to all particles in the field.
[b] Maximum peak of 3-Gaussian fit.

(∼6 kpc). As the distance is increased, the particle's velocity increases since both v_ϕ and $v_{\rm R}$ are increasing and also because the velocity vector is coincident with the line of sight. The highest velocity particles are approaching their pericentre occurring on the short axis of the bar at a distance of ∼8 kpc, very close to $R_\odot$. This picture is consistent with our interpretation of the high velocity peaks in Bulge fields being due to the motions of resonant 2:1 bar orbits.

Can we use this insight to constrain the viewing angle of the bar, using the information on how the velocity peaks vary with Galactic position? In Figure 4, the black stars and dots represent the locations of the peaks found by Nidever et al. (2012). Overplotted as blue dots and red stars are the positions of the peaks from our models. Specifically, the blue dots are derived from the Gaussian mixture models for the 2:1 resonant orbits, whilst the red stars are extracted from χ^2 fits to all the particles in the field. It is clear that, although no single choice of viewing angle reproduces all the data, the trends in the velocity peaks are well-reproduced for bar angles $\sim 15^\circ$.

The fields with the largest deviations are the ones with the highest longitude, for which our simple picture probably breaks down. Although the peaks in these fields are quite pronounced, they systematically lie at lower values compared to the data. This could be due to one of two possible scenarios. Firstly, being at high longitudes, particles in these fields feel a significant cumulative effect of the shallower potential. The high velocity particles in fields with $l \geq 10^\circ$ are at pericentre between 1.5 and 2.0 kpc along the short axis of the bar. We expect the potential to be somewhat shallower since the pure disc simulation is absent of a gaseous component and live halo that may relax into a more concentrated configuration after the formation of the bar. However, the simulation has been shown to be in good agreement with the kinematics observed by BRAVA Shen et al. (2010), even as far out as $l = 10^\circ$. A good match is made to the mean velocities and velocity dispersions, so that the comparison is made to the data through the whole line of sight. As we've shown above (Figure 3, bottom right), the high velocity peaks correspond to a limited range in distance. That the deviation from the observed peaks increases with l is another indication that a somewhat shallow potential is the cause.

Another possible scenario is that the peaks are in fact caused by another family of resonant orbits. We have checked the other major families in the bar, the 3:1 and 5:2 families. They do generate strong peaks in these fields but, as with the 2:1 orbits, the high velocity peaks are at systematically lower values (combinations of the 2:1, 3:1 and 5:2 orbits also result in peaks with low values). However, other higher order resonances may also be important in these regions. As mentioned in Nidever et al. (2012), the high velocity peaks are unlikely to be due to tidal streams. Although the Sagittarius stream lies close by on the plane of the sky, the high velocity stars show no preference for magnitude or metallicity and, in any case, the stream stars are not expected to appear in large numbers (Law & Majewski 2010).

Another way of synthesizing this information is presented in Figure 5, which shows how the location of the high velocity peak varies with assumed viewing angle of the bar. The observational data for each field are represented by the horizontal blue line, and suggest viewing angles between 10° and 25°. Some scatter is expected, as the N-body model does not exactly reproduce the three-dimensional density of the inner Galaxy and the kinematical properties are subject to numerical shot noise.

4. DISCUSSION AND CONCLUSIONS

We have shown that the high velocity peaks seen in APOGEE commissioning data (Nidever et al. 2012) may be explained by the presence of a large family of 2:1 resonant orbits in the Galactic bar. These orbits are elongated along the bar's major axis, and must support the distended shape of the bar to provide its backbone. When viewed at bar angles in the range $10^\circ < \theta_{\rm bar} < 25^\circ$, the 2:1 orbits naturally give rise to secondary peaks in the line of sight velocity distributions at $v_{\rm los} \sim 200$ km s^{-1}. We have provide a pictorial explanation of this phenomenon.

Our interpretation is open to the objection that the method is not fully self-consistent. We have shown that the population of 2:1 orbits can generate the kinematic features to explain the data of Nidever et al. (2012), but we have allowed the normalization of the density in these orbits to vary independently of the N body model from which they were extracted. This though is unlikely to be a serious concern, as the range of self-consistent equilibria for bars is wide and solutions will exist using different relative populations for the orbital families that comprise the bar. As we have mentioned above, the other resonant orbit families also produce rich structure in their velocity distributions. If we combine the 2:1, 3:1 and 5:2 orbits in our distributions, the high velocity peaks (which are somewhat more obscured) are dominated by the 2:1 orbits and so follow the trends outlined above to suggest $\theta_{\rm bar} \approx 15^\circ$.

Another important consideration is the range of distances probed by observations. Given the non-uniform distribution of dust towards the Galactic Bulge, it is certain that different fields are reaching different distances. Indeed the range of distances reached may vary significantly through just one field. The lower right panel of Figure 3 shows that the highest velocity stars are placed at a distance close to $R_\odot$. It is clear then that distance has an important role in shaping the velocity distributions.

Some issues remain about the high velocity peaks. The first is why symmetry is not seen between positive and negative latitude fields. Peaks are observed in the field at (4.3,-4.3) but not in the field at (4.3,4.3), the same goes for the fields at (5.7,-2) and (5.7,2). The obvious explanation for such a difference is that the distances being probed differs between north and south. It is known that extinction in the north is greater than in the south (Gonzalez et al. 2012), which offers

a possible explanation for the disparity. However, according to APOGEE estimates, although the average extinction is indeed greater for the field at (4.3,4.3) than for the field at (4.3,-4.3), the opposite is the case for the fields at (5.7,2) and (5.7,-2). Another point to consider is that in the plane, where extinction is highest, strong peaks are seen. A possible explanation here is that the number density of bar supporting orbits is higher in these regions. In any case, the extinction data is at its most uncertain in the plane of the disc, making the previous suggestions purely speculative.

The second major concern is the differences between different Bulge surveys. The BRAVA, ARGOS and GIBS surveys don't report the detection of cold streams in the Bulge. The presence of the peaks in the APOGEE data should be resolutely confirmed on analysis of the post–commissioning data. That the cold peaks are seen in one survey and not the others provides a possible clue as to the nature of bar supporting orbits. The clue lies in the different observing strategies and selection functions for the data. The color selections are similar, with each survey using cuts on $J-K$ color, but the magnitude ranges are not the same. These surveys each cover different footprints (with only APOGEE and GIBS observing a significant number of fields below $|l| = 4^\circ$), and also observe different types of stars (GIBS & ARGOS: mainly red clump; APOGEE & BRAVA: mainly M-giants). Since the targets that make up each survey differ in spatial (survey footprint, distance), temporal (ages) and chemical (color, magnitude) attributes, the question of why cold streams are seen in one survey and not others is certainly challenging (it should also be noted that the observing strategy may be selecting stars with a low velocity dispersion, thereby thinning the overall distributions to reveal the cold peak). A better question might be whether APOGEE has stumbled on a selection strategy that preferentially selects bar stars, and if so, can the strategy be shown to be consistent with chemical and dynamical models of the Galactic Bulge?

The authors acknowledge financial support from the CAS One Hundred Talent Fund and NSFC Grants 11173002, 11333003, 11322326 and 11073037. This work was also supported by the following grants: the Gaia Research for European Astronomy Training (GREAT-ITN) Marie Curie network, funded through the European Union Seventh Framework Programme (FP7/2007-2013) under grant agreement no 264895; the Strategic Priority Research Program "The Emergence of Cosmological Structures" of the Chinese Academy of Sciences, Grant No. XDB09000000; and the National Key Basic Research Program of China 2014CB845700. This work made use of the super-computing facilities at Shanghai Astronomical Observatory.

REFERENCES

Babusiaux, C., Katz, D., Hill, V., et al. 2014, *A&A*, 563, A15
Blitz, L., & Spergel, D. N. 1991, *ApJ*, 379, 631
Cao, L., Mao, S., Nataf, D., Rattenbury, N. J., & Gould, A. 2013, *MNRAS*, 434, 595
Dehnen, W. 1999, *ApJ*, 524, L35
—. 2000, *AJ*, 119, 800
Dwek, E., Arendt, R. G., Hauser, M. G., et al. 1995, *ApJ*, 445, 716
Englmaier, P., & Gerhard, O. 1999, *MNRAS*, 304, 512
Evans, N. W., & Belokurov, V. 2002, *ApJ*, 567, L119
Gonzalez, O. A., Rejkuba, M., Zoccali, M., et al. 2012, *A&A*, 543, A13
Law, D. R., & Majewski, S. R. 2010, *ApJ*, 714, 229
Li, Z.-Y., & Shen, J. 2012, *ApJ*, 757, L7
Li, Z.-Y., Shen, J., Rich, R. M., Kunder, A., & Mao, S. 2014, ArXiv e-prints, arXiv:1401.2996
López-Corredoira, M., Cabrera-Lavers, A., Mahoney, T. J., et al. 2007, *AJ*, 133, 154
Molloy, M., Smith, M. C., Shen, J., & Evans, N. W. 2015, ApJ in press; ArXiv:1412.4689, arXiv:1412.4689
Nataf, D. M., Udalski, A., Gould, A., Fouqué, P., & Stanek, K. Z. 2010, *ApJ*, 721, L28
Ness, M., & Freeman, K. 2012, in European Physical Journal Web of Conferences, Vol. 19, European Physical Journal Web of Conferences, 6003
Ness, M., Freeman, K., Athanassoula, E., et al. 2012, *ApJ*, 756, 22
—. 2013, *MNRAS*, 432, 2092
Nidever, D. L., Zasowski, G., Majewski, S. R., et al. 2012, *ApJ*, 755, L25
Pietrukowicz, P., Kozlowski, S., Skowron, J., et al. 2014, ArXiv e-prints, arXiv:1412.4121
Rattenbury, N. J., Mao, S., Sumi, T., & Smith, M. C. 2007, *MNRAS*, 378, 1064
Rich, R. M., Reitzel, D. B., Howard, C. D., & Zhao, H. 2007, *ApJ*, 658, L29
Robin, A. C., Marshall, D. J., Schultheis, M., & Reylé, C. 2012, *A&A*, 538, A106
Saito, R. K., Zoccali, M., McWilliam, A., et al. 2011, *AJ*, 142, 76
Shen, J., Rich, R. M., Kormendy, J., et al. 2010, *ApJ*, 720, L72
Udalski, A., Szymanski, M., Stanek, K. Z., et al. 1994, , 44, 165
Wegg, C., & Gerhard, O. 2013, *MNRAS*, 435, 1874
Weiner, B. J., & Sellwood, J. A. 1999, *ApJ*, 524, 112
Wyrzykowski, Ł., Rynkiewicz, A. E., Skowron, J., et al. 2015, *ApJS*, 216, 12
Zoccali, M., Gonzalez, O. A., Vasquez, S., et al. 2014, *A&A*, 562, A66